Considerations for an 8-inch Wafer-Level CMOS Compatible AlN Pyroelectric 5–14 μm Wavelength IR Detector Towards Miniature Integrated Photonics Gas Sensors

Doris K. T. Ng, Guoqiang Wu, *Member, IEEE*, Tan-Tan Zhang, Linfang Xu, Jianbo Sun, Wing-Wai Chung, Hong Cai, Qingxin Zhang, and Navab Singh

***Abstract*— CMOS compatibility and 8-inch manufacturability have been highly desired in MEMS technology. In this article, we demonstrate a MEMS pyroelectric IR detector using CMOS compatible AlN and 8-inch semiconductor wafer technology. This AlN pyroelectric detector detects IR over wavelength ranging from 5 μm to 14 μm. In addition, this detector is designed to have added mechanical stiffness for improved device integrity. The detectors are fabricated with different sensing area dimensions to compare their performance. The best performing detector has an *NEP* $\sim$ 8.87 x 10^{-9} W/$\sqrt{Hz}$ and *D** $\sim$ 6.04 x 10^6 cm$\sqrt{Hz}$/W. These pyroelectric detectors are designed and built with the consideration to enable ease of monolithic integration with other components to form an integrated gas sensor system. This includes enabling detection of illumination from the front side and using an absorber stack that consists of CMOS dielectric layers. Subsequently, they will form a crucial part of the architectures for miniature photonics-based gas sensors. Their performance is a first step towards 8-inch wafer level CMOS-compatible manufacturable photonics gas sensors. [2020-0157]**

***Index Terms*— Aluminum compounds, CMOS technology, infrared detectors, pyroelectric devices, microelectromechanical devices, optical sensors.**

I. Introduction

PYROELECTRIC detectors are thermal detectors that operates at room temperature. They make use of temperature fluctuations to produce spontaneous polarization in the pyroelectric sensing material [1], resulting in an output electrical signal. Other than the ability to operate without external cooling which helps to reduce the system footprint considerably, advantages of pyroelectric detectors include wide spectral of operation, covering infrared (IR) wavelength range and no requirement for bias current. Some applications of pyroelectric detectors [2], [3] are intruder alarms, fire alarms, pollution monitoring and gas analysis, radiometers, laser detectors and pyroelectric thermal imaging [4]. Materials used for pyroelectric detection and effect include Lead Zirconate Titanate (PZT) [5]–[7], Poly Vinylidene Fluoride (PVDF) [8], Lithium Tantalate ($LiTaO_3$) [9], Lead Tantalate ($PbTiO_3$) [10].

In recent years, Aluminum Nitride (AlN) material is gaining significant interest [2], [3], [11], [12] as a pyroelectric material for uncooled thermal IR detection. Characteristics of AlN material include high Curie temperature ($\sim$2000°C) [13], [14], complementary metal-oxide-semiconductor (CMOS) compatibility and being free from lead (Pb) and lithium (Li). High Curie temperature opens up the opportunity for the detector to function at a higher temperature environment while still maintaining its material properties as compared to materials with lower Curie temperature such as poly(vinylidene fluoride-trifluorethylene) (P(VDF-TrFE)) which has a Curie temperature of around 100°C [15]. CMOS compatibility allows for monolithic integration of micro-electro-mechanical system (MEMS) pyroelectric devices with other CMOS devices over 8-inch wafer for increased manufacturability, throughput and reduced footprint. There have been many studies on AlN and enormous efforts to determine its pyroelectric coefficient and material properties [16]–[20].

Most recently, there have been reports on progress of integrated mid-IR optical gas sensors [21], leveraging on the absorption characteristics of gas when interacting with light at certain wavelengths for miniature, low cost and low power devices. Specific to AlN pyroelectric detectors, there have been recent demonstrations on AlN pyroelectric near-IR [22] and mid-IR to far-IR [23] detectors, and AlN pyroelectric mid-IR detector for carbon dioxide (CO_2) gas sensing [24]. As most gases absorb electromagnetic radiation at different IR wavelengths, pyroelectric detector could be used towards detection of gas and its concentration by analyzing the electrical output signal observed at the gas absorption wavelength. The mid-IR

Manuscript received May 12, 2020; revised July 30, 2020; accepted August 6, 2020. Date of publication August 17, 2020; date of current version October 7, 2020. This work was supported by the Agency for Science, Technology, and Research under Grant IAF-PP A1789a0024. Subject Editor C. Lee. *(Corresponding author: Doris K. T. Ng.)*

Doris K. T. Ng, Tan-Tan Zhang, Linfang Xu, Wing-Wai Chung, Hong Cai, Qingxin Zhang, and Navab Singh are with the Institute of Microelectronics, Agency for Science, Technology and Research (A∗STAR), Singapore 138634 (e-mail: Doris_NG@ime.a-star.edu.sg).

Guoqiang Wu was with the Institute of Microelectronics, Agency for Science, Technology and Research (A∗STAR), Singapore 138634. He is now with The Institute of Technological Sciences, Wuhan University, Wuhan 430072, China.

Jianbo Sun was with the Institute of Microelectronics, Agency for Science, Technology and Research (A∗STAR), Singapore 138634. He is now with HiSilicon Technologies Company Ltd., Shenzhen 518129, China.

Color versions of one or more of the figures in this article are available online at http://ieeexplore.ieee.org.

Digital Object Identifier 10.1109/JMEMS.2020.3015378

This work is licensed under a Creative Commons Attribution 4.0 License. For more information, see https://creativecommons.org/licenses/by/4.0/

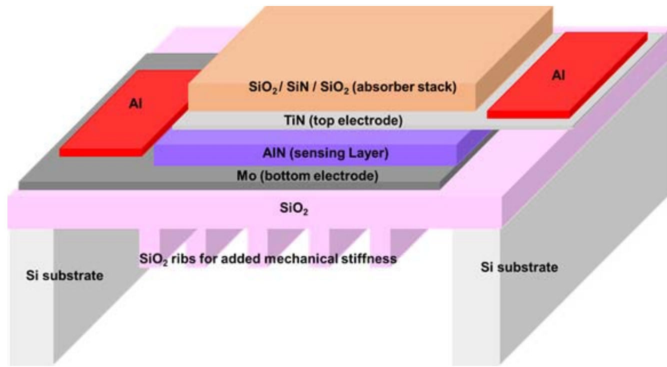

Fig. 1. Schematic of the pyroelectric detector showing the structure layers. The absorber stack is the top most layer and AlN sensing layer is between the top and bottom electrode. An array of SiO_2 ribs is fabricated under the bottom electrode to increase the mechanical stiffness of this membrane device. Al is used for the metal contacts.

wavelength range from 2 μm to 20 μm has many characteristic absorption lines who could help in gas sensing [21].

In this article, we present a CMOS compatible AlN-based 5 μm to 14 μm wavelength IR pyroelectric detector with design considerations on maximizing absorption, increased mechanical stiffness and output signal. In order to match our device fabrication process as close as possible with CMOS-MEMS industry standards, these detectors are fabricated using micro-electro-mechanical system (MEMS) 8-inch wafer technology. In addition, AlN sensing layer of different sizes are also fabricated and measured to determine the optimal sensing size for this detector. The work here demonstrates functional pyroelectric detectors that is designed and built with considerations to enable ease of integration with other components to form an integrated gas sensor system. This includes allowing thermal sensing from the front surface, using an absorber stack that consists of CMOS dielectric layers and determining the optimal sensing size. This CMOS compatible pyroelectric detector using wafer level fabrication technology can thus be easily integrated [25] with an emitter [26] and waveguide [27]–[29], enabling realization of miniature photonics gas sensor systems.

II. Design Considerations

Figure 1 shows a schematic of our pyroelectric detector design layer structure. The pyroelectric sensing material used is AlN sandwiched between bottom electrode molybdenum (Mo) and top electrode Titanium Nitride (TiN). As TiN has fairly low thermal conductivity (reported around 3 $Wm^{-1}K^{-1}$ [30] to 12 $Wm^{-1}K^{-1}$ [31]), we design our TiN top electrode to be thin (thickness ~50 nm) so that this layer will not eventually become a serious thermal barrier. The metal contacts used is aluminum (Al).

On top of this stack is an IR absorber structure of silicon dioxide - silicon nitride - silicon dioxide (SiO_2-SiN-SiO_2) thin film stacks. The role of the absorber is to maximize incident thermal radiation absorption. The thermal energy received by the absorber will later be transferred to the pyroelectric AlN layer. AlN thin films of 100 nm thickness have been reported to have high transmission ($>90\%$) and low reflection ($<10\%$) from wavelength range from around 1 μm to 3 μm [9], hence absorption is quite low over this wavelength range. To compensate for this, an absorber on top of AlN is desired. In this case, we design the absorber above the top electrode. We consider using CMOS dielectric stack as the absorber consisting of SiN sandwiched between 2 layers of SiO_2. The intention is to create absorption by destructive interference between reflected and incident waves in this dielectric stack. Three layers of dielectric films are chosen to broaden the absorption bandwidth. SiO_2-SiN-SiO_2 stack is chosen as SiO_2 and SiN dielectric films are CMOS-compatible and are quite well-developed in terms of process and quality. In addition, the top SiO_2 layer could also help to protect the underlying SiN layer from XeF_2 etch process during the Si substrate release step as XeF_2 will react with SiN [32] during the etching process if not protected. On top of all these, the SiO_2-SiN-SiO_2 absorber stack allows us to fabricate the pyroelectric detector as a device that could function both as a component by itself and at the same time allow for ease of monolithic integration with the emitter and waveguide. The thermal energy generated upon incident IR radiation will result in polarization changes in the pyroelectric AlN material which in turn will generate an electrical signal.

To create thermal isolation for the detector to sense optimal temperature change, the detector stack structure will be in the form of a thin membrane with the backside silicon (Si) substrate removed. Fabricating this is especially challenging and could often result in membrane breakage, hence decreasing yield of working devices. To reduce the incidents of membrane breakage, we design an SiO_2 rib array at the mechanical support layer underneath the bottom Mo electrode (Figure 1). This is done to increase the mechanical stiffness of the membrane and ensure adequate support for the film stack. The SiO_2 ribs are of width 1 μm and length 5 μm. As low pressure chemical vapor deposition tetraethyl orthosilicate (LPCVD TEOS) process is used to fill the trenches, a trench width of 1 μm would ensure that the trench depth of 5 μm is filled sufficiently to form the SiO_2 ribs structure. If the trench width is too wide, the filling process will take very long and results in high process cost. High density of ribs is required to improve mechanical robustness of the membrane but should not introduce too much additional stress on the detector membrane. In this work, we choose a pitch of 10 μm between rib to rib.

To obtain maximum output signal, we also consider the pyroelectric current equation [24], [33] defined as follows:

$$i = A\rho \frac{dT}{dt}, \tag{1}$$

where i is the pyroelectric current, A is the sensing area of the detector, ρ is the pyroelectric coefficient of AlN and dT/dt is the rate of change of temperature with time. Based on (1), in order to achieve maximum pyroelectric current, a large sensing area (A) and increase rate of change of temperature with time (dT/dt) are desired. However, these 2 factors can form a trade-off. If the sensing area (A) increases indefinitely, there will come a point when the temperature response time (dT/dt) reduces due to the large sensing area. Hence, a balance between both the sensing area (A) and

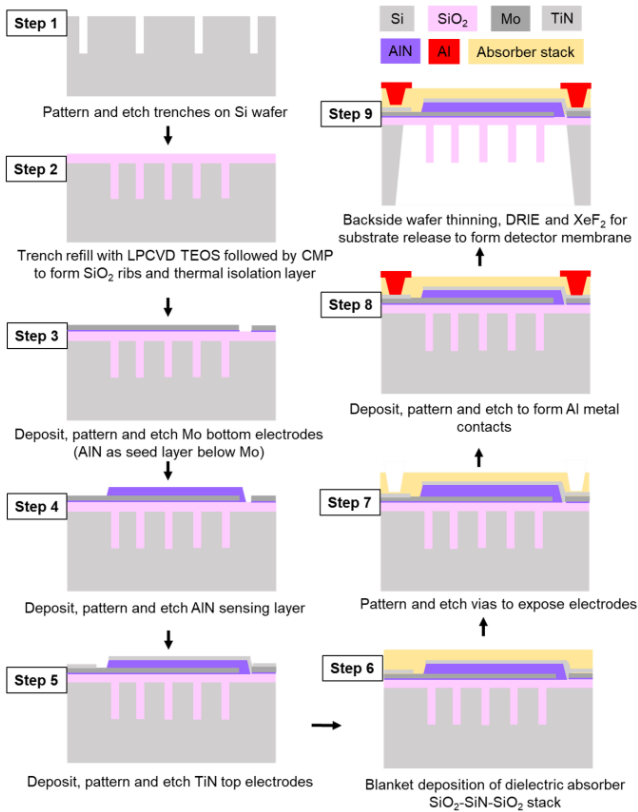

Fig. 2. Process flow schematic to illustrate the fabrication process. Trenches are formed and refilled followed by CMP to create the SiO_2 ribs and thermal isolation layer (Step 1 – 2). Step 3 – 5 shows pattern formation of the Mo bottom electrode, AlN sensing layer and TiN top electrode. Subsequently, at Step 6, an absorber consisting of SiO_2-SiN-SiO_2 stack is blanket deposited followed by via opening and Al metallization (Step 7 – 8). The final Step 9 involves backside wafer thinning, DRIE and XeF_2 for substrate release to form the detector membrane.

temperature response time *dT/dt* is required. In this article, AlN pyroelectric detectors with 4 different sensing areas are designed and measured to observe how the effect of membrane size will affect the output current.

III. Experimental

The fabrication process is done on 8-inch wafer-level scale, to match CMOS-MEMS industry standards as close as possible. Figure 2 shows a schematic integration flow to illustrate the fabrication process. We start with an 8-inch Si wafer. Arrays of trenches, 1 μm wide are patterned and etched into the Si wafer for 5 μm. This is followed by the deposition of LPCVD TEOS of around 1 μm thick to form the thermal isolation layer and the SiO_2 ribs each of 1 μm wide and 5 μm long for added mechanical stiffness. Chemical mechanical polishing (CMP) is then done on this SiO_2 layer to create a flat surface. The respective stack layers were deposited, patterned and etched to form the pyroelectric detector structure. As seen from Figure 2, these layers are Mo, AlN and TiN. This is followed by a blanket deposition of the absorber stack. Mo and TiN form the bottom and top electrodes with thicknesses of 150 nm and 50 nm respectively. Underneath the Mo bottom electrode is a thin layer (thickness $\sim$ 20 nm) of AlN that acts as a seed layer for Mo. The pyroelectric sensing material

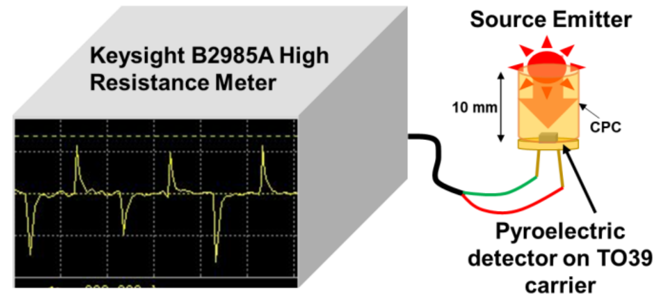

Fig. 3. Schematic of the test measurement setup with a fabricated pyroelectric detector wire-bonded onto a TO-39 header and connected to a high precision current meter. Thermal source comes from a thermal MEMS emitter irradiating the detector from the top. Image on the left is a screenshot of the output waveform obtained.

used is AlN deposited at a temperature of around 200°C for a thickness of 1 μm. The absorber stack consists of SiO_2-SiN-SiO_2 structure. The stack layers' thicknesses are 530 nm for the first SiO_2 layer located on top of TiN, 230 nm for the SiN layer and 450 nm for the final SiO_2 layer. Vias are then opened to expose the electrodes surfaces and Al is deposited on Mo and TiN to form the contact pads. The thickness of Al is 1 μm. Finally, the backside of the Si substrate is thinned down to 500 μm at wafer level. After a hard mask oxide layer of 1 μm deposition and patterning, silicon is removed from wafer backside by combined deep reactive ion etching (DRIE) and Xenon difluoride (XeF_2) etch. Thermal isolation is created so that the thermal energy detected by the detector will not be lost by thermal conduction through the Si substrate. The fabricated pyroelectric detector device is in the form of a membrane connected to the Si substrate. The wafer is then diced into die-form where each die consists of a pyroelectric detector component.

The fabricated pyroelectric detectors are first optically measured using a Fourier Transform Infrared (FTIR) spectrometer to observe the absorption spectra at wavelength from 5 μm to 14 μm. Each die is then packaged by wire-bonding it to a transistor outline (TO)-39 header and connected to a high precision current meter (Keysight B2985A High Resistance Meter) which can measure current down to 0.01 fA, allowing us to extract the output current directly without the need of a circuit board for current-to-voltage conversion.

Figure 3 shows a schematic of the test setup used to measure the output from the AlN pyroelectric detector. The source emitter is a commercially bought thermal MEMS based IR component (Axetris EMIRS50 AT06V). A compound parabolic concentrator (CPC) is mounted on the source emitter to provide collimated light to the detector. The detector is fitted directly on the other end of the CPC to receive the emission from the source emitter. The length of the CPC is 10 mm, therefore the source and detector are set apart by the CPC at a distance of 10 mm. The source emitter power irradiating on the detector is estimated to be $\sim$ 0.01 mW based on the data sheet provided for Axetris EMIRS50 AT06V emitter and the distance between the source emitter and detector. The source emitting signal is set at a square wave frequency of 1 Hz. The output spectrum, peak current and rising time are measured

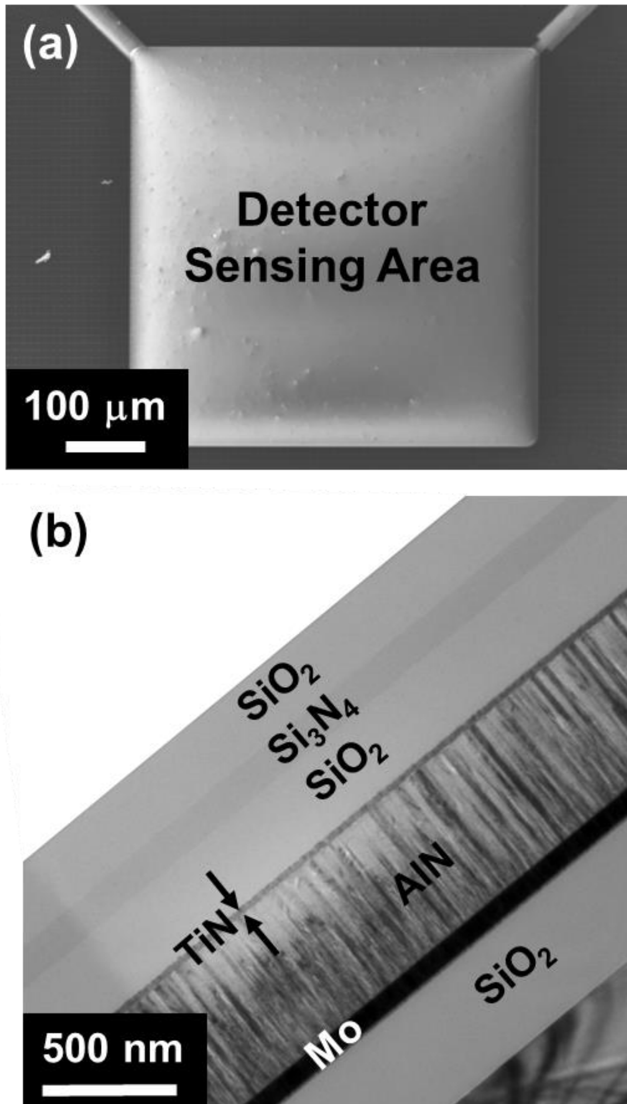

Fig. 4. a) Top-view SEM image of the fabricated detector before substrate release which shows the top surface of the sensing area and b) Cross-sectional TEM image of the fabricated detector stack which shows the layers fabricated. Each layer thickness is measured. The AlN layer is also observed to have columnar-like structure, an indication of c-axis orientation.

by the current meter. The image on the current meter is a screenshot of an output waveform of the pyroelectric detector when irradiated by the IR source.

IV. Results and Discussion

Figure 4a shows the top view scanning electron microscopy (SEM) image of a fabricated pyroelectric detector before substrate release with sensing dimension of 500 μm by 500 μm. SiO_2 rib array is observed at the background next to the detector sensing area. The 2 strips at the top of the image are the top and bottom electrode lines. Figure 4b shows the cross-sectional transmission electron microscopy (TEM) image with the different layers defined. The thicknesses measured by the TEM are as follows: first bottom layer of SiO_2 has measured thickness of 760 nm, Mo bottom electrode has layer thickness of 144 nm, AlN sensing layer has thickness 1.014 μm, TiN top electrode layer has thickness 47.3 nm and absorber stack of SiO_2-SiN-SiO_2 has layer thicknesses of 527 nm, 221.2 nm and 436.6 nm respectively. In Fig. 4, we can also see that the cross-sectional AlN layer shows columnar-like structures, indicating that AlN layer is c-axis oriented. Hence pyroelectric coefficient of this AlN layer is around 6-8 μC/(m^{2}K) [18].

Absorption spectra of the pyroelectric detectors are measured experimentally using Shimadzu AIM-9000 FTIR Spectrometer and numerically simulated using Finite Difference Time-Domain (FDTD) software. In FTIR, we first measure the transmittance (T) of the entire detector stack followed by reflectance (ρ). Absorbance (α) is then calculated based on the following equation:

$$\alpha = 1 - \rho - \mathrm{T} \tag{2}$$

Figure 5a shows measured reflectance and transmittance spectra of the entire detector stack over the wavelength range from 2.25 μm to 14 μm. It can be seen that reflectance is quite high at shorter wavelengths less than 5 μm, peaked ($>90\%$) at around wavelength 4 μm. Transmittance is in general less than 6% transmission and reduces further at longer wavelengths.

Figure 5b shows the experimental FTIR absorption (%) spectrum calculated based on the FTIR transmission (%) and reflection (%) spectra (black line). Due to the higher reflection (%) and transmission (%) at wavelengths less than 5 μm, absorption (%) is lower at short wavelengths and higher at longer wavelengths (5 μm to 14 μm). From Fig. 5b, we observe absorption $> 60\%$ from wavelength range of 5 μm to 14 μm in our experimental FTIR spectrum. Absorption also goes up to 80% at the wavelength of around 6.5 μm and 100% at wavelength of around 10.5 μm and 13.5 μm respectively. High absorption in the detector stack could contribute to more sensitive gas sensing at the specific gas absorption wavelength. The wavelength ranging from 5 μm to 14 μm is important as it covers applications from environmental monitoring to industrial process control and medical diagnosis [21].

A 2D FDTD simulation based on the fabricated detector stack using the layer thickness measured by TEM is also presented in Fig. 5b (blue line). The material parameters used for SiO_2 and TiN are from the FDTD material database, namely 'Glass-Palik' and 'TiN-Palik' respectively. For AlN, the material parameters used in FDTD simulation are based on experimental data from our in-house deposited AlN film, measured using an ellipsometer with refractive indices and absorption coefficients obtained across wavelengths ranging from 1.7 μm to 40 μm. Material parameters used for SiN and Mo are extracted from literature [34], [35]. In FDTD simulation, the source is set incident on the absorber layer and transmission and reflection are calculated simultaneously. Absorption is calculated using (2). The FDTD simulation shows overall similar trend with the FTIR absorption spectrum with absorption above 60% over this wavelength range of 5 μm to 14 μm. The difference observed between FTIR experimental spectrum and FDTD simulated spectrum could be due to the different material parameters (refractive indices and absorption coefficients) used in FDTD simulation compared to that of the actual material deposited.

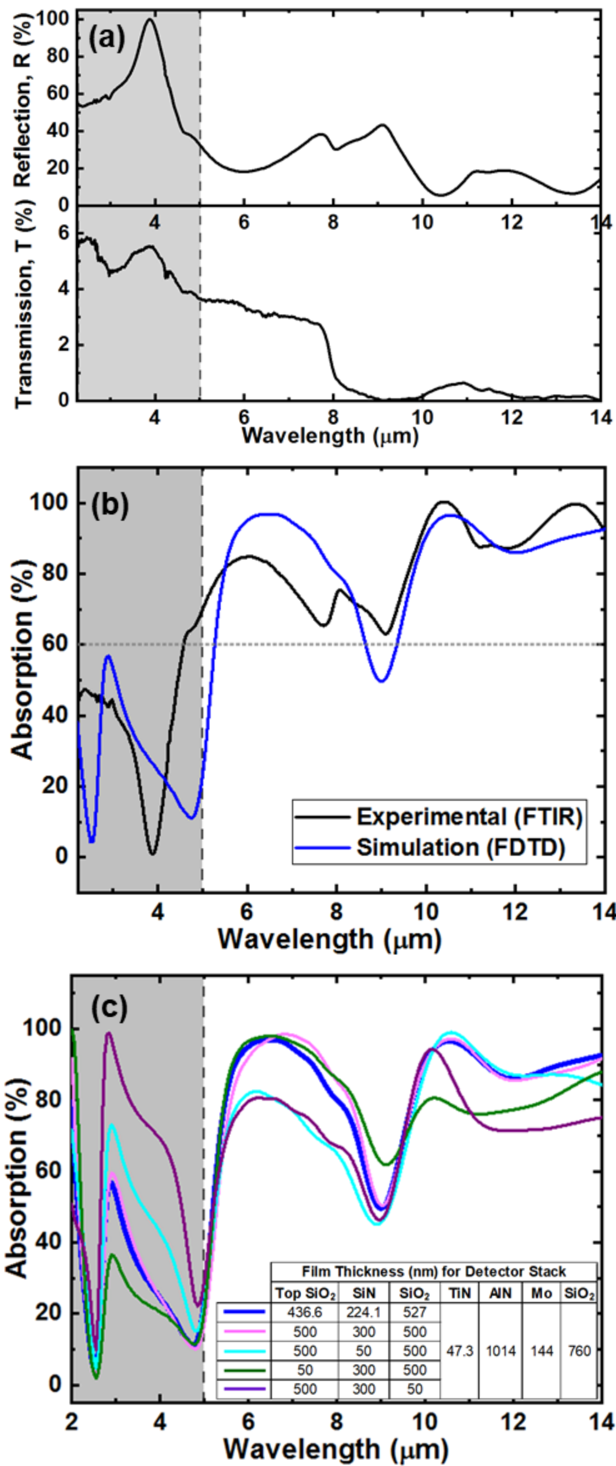

Fig. 5. Optical spectra of the pyroelectric detector stack device. a) FTIR measurement on the reflection and transmission spectra of fabricated pyroelectric detector, b) Absorption spectrum (BLACK line) of the fabricated pyroelectric detector calculated from the FTIR reflection and transmission data, simulated absorption spectrum (BLUE line) using FDTD software and c) simulated absorption spectra for the pyroelectric detector stack with absorber of various layer thicknesses using FDTD software. The BLUE line is based on fabricated absorber layer thicknesses. The MAGENTA line is based on rounded-off absorber layer thicknesses for ease of comparison when varying absorber layer thickness.

As the FDTD simulated spectrum in Fig. 5b shows a dip in absorption at around 9 μm wavelength, we further investigate the effect of the absorber layer thicknesses on the absorption spectrum of the entire detector stack. Figure 5c shows the simulated absorption spectra of the pyroelectric detector stack with varying SiO_2-SiN-SiO_2 absorber layer thicknesses. By keeping the thickness of the other layers constant, we change only the thickness of the SiO_2 and SiN in the absorber stack. For reference, simulated absorption spectrum of the detector stack based on the actual fabricated detector stack thicknesses is indicated by the blue spectrum. We start with an absorber stack thicknesses closed to the actual fabricated absorber – 500 nm SiO_2, 300 nm SiN, 500 nm SiO_2 (magenta spectrum). As the thickness of the center SiN layer reduces from 300 nm to 50 nm (cyan spectrum), the absorption drops at 9 μm wavelength. Another observation is that when the SiO_2 layer (layer on TiN top electrode) reduces from thickness of 500 nm to 50 nm (purple spectrum), absorption drops at 9 μm wavelength and longer wavelengths (11 μm to 14 μm). Nevertheless, this thinner SiO_2 layer (layer on TiN top electrode) does help to increase absorption at lower wavelengths (2 μm to 5 μ m). For the top-most SiO_2 layer, it should not be too thin as it will reduce the absorption at short (2.5 μm to 5 μm) and long wavelengths (11 μm to 13 μm) when its thickness reduces to 50 nm (green spectrum). Depending on applications and wavelength of interest, the absorber stack layer thicknesses can be adjusted accordingly. In this work, we focus on wavelength range from 5 μm to 14 μm in which the fabricated structure gives an experimental absorption spectrum above 60%.

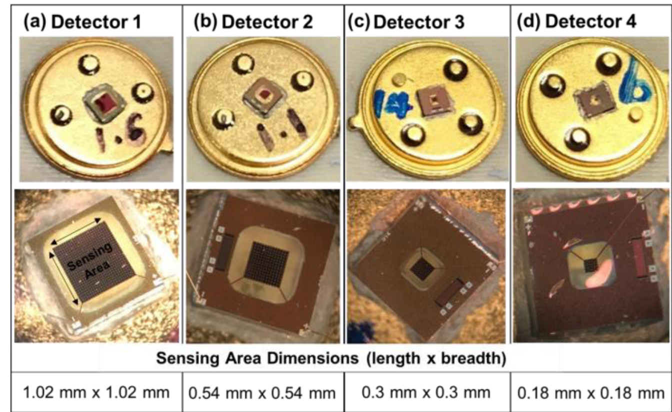

Fig. 6. Photos with their respective microscopy images of the detector devices showing different sensing areas. a) Detector 1 with area of 1.04 mm^2 (1.02 mm $\times$ 1.02 mm), b) Detector 2 with area of 0.29 mm^2 (0.54 mm $\times$ 0.54 mm), c) Detector 3 with area of 0.09 mm^2 (0.3 mm $\times$ 0.3 mm) and d) Detector 4 with area of 0.03 mm^2 (0.18 mm $\times$ 0.18 mm).

Figure 6 shows the photo and microscopy images of 4 fabricated pyroelectric detectors with 4 different sensing area sizes. The sensing area sizes are Fig. 6a) Detector 1 with area of 1.04 mm^2, Fig. 6b) Detector 2 with area of 0.29 mm^2, Fig. 6c) Detector 3 with area of 0.09 mm^2 and Fig. 6d) Detector 4 with area of 0.03 mm^2. These detectors are wire-bonded to TO-39 header and the microscopy images show clearly that the Si substrate underneath the AlN sensing element is removed.

Figure 7a-d shows the measured output current spectra of these 4 pyroelectric detectors. It can be seen that Detector 2

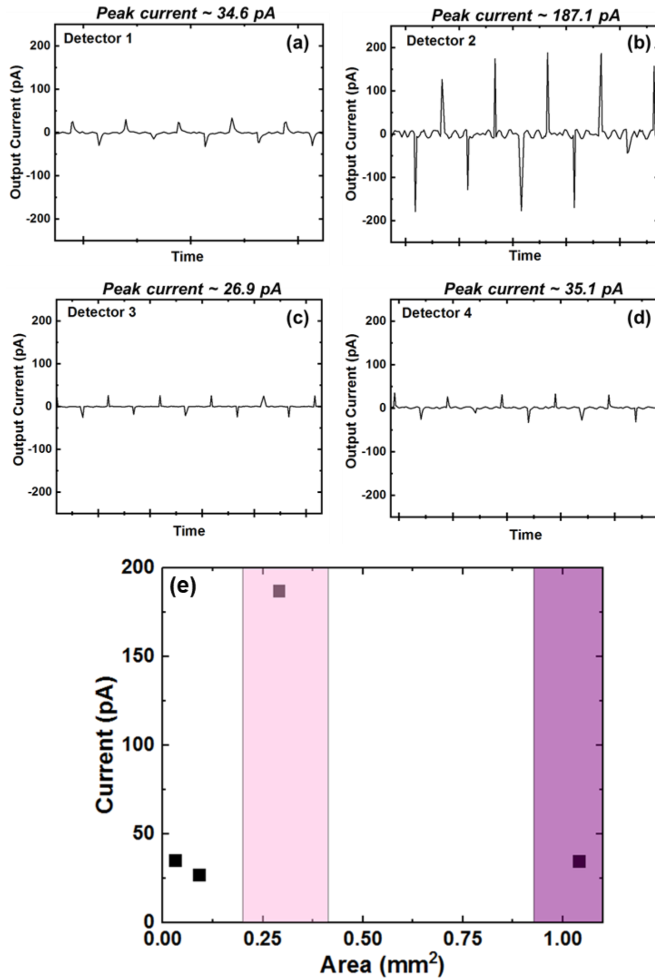

Fig. 7. Measured output current of 4 pyroelectric detectors with different size of sensing areas a) Detector 1 with area of 1.04 mm^2 showing peak output current of 34.6 pA, b) Detector 2 with area of 0.29 mm^2 showing peak output current of 187.1 pA, c) Detector 3 with area of 0.09 mm^2 showing peak output current of 26.9 pA and d) Detector 4 with area of 0.03 mm^2 showing peak output current of 35.1 pA. e) Graph of peak output current against sensing areas indicating region where sensing area (A) dominates and region where rate of change of temperature with time ($\frac{dT}{dt}$) dominates.

(Fig. 7b) gives the best performance with peak output current ~187.1 pA. Rise time ~ 20 ms and dark current ~ 1 pA. As defined by (1), pyroelectric current is directly proportional to size of the sensing area and rate of change of temperature with time. There is however a trade-off between these 2 factors. The sensing area cannot increase indefinitely to obtain maximum current output. There will come a point where further increase in the sensing area causes a decrease in the output current. This is because the rate of change of temperature with time has become the dominating factor and it takes a much longer time per unit change in temperature. This is observed experimentally and shown in Figure 7e which shows a plot of the output current against the sensing area. There is an increase in output current when the sensing area is 0.29 mm^2 compared to when the sensing area is 0.09 mm^2. However, output current decreases when the sensing area increases further to 1.04 mm^2. Hence we can postulate that the sensing area (A) is the dominating factor at region around

TABLE I

SUMMARY OF THE PERFORMANCE OF OUR AlN PYROELECTRIC DETECTORS OF DIFFERENT SENSING AREAS. THE BEST PERFORMANCE IS OBTAINED FOR DETECTOR 2 WITH SENSING AREA OF 0.29 mm^2

Pyroelectric Detector ID	**Size of AlN Sensing Area, *A* (mm^2)**	**Responsivity, *R* (A/W)**	**Noise Equivalent Power, *NEP* (W/$\sqrt{\text{Hz}}$)**	**Specific Detectivity, *D** (cm$\sqrt{\text{Hz}}$/W)**
Detector 1	1.04	5.43×10^{-6}	4.80×10^{-8}	2.12×10^{6}
Detector 2	**0.29**	$\mathbf{2.94 \times 10^{-5}}$	$\mathbf{8.87 \times 10^{-9}}$	$\mathbf{6.04 \times 10^{6}}$
Detector 3	0.09	4.22×10^{-6}	6.18×10^{-8}	4.79×10^{5}
Detector 4	0.03	5.52×10^{-6}	4.73×10^{-8}	3.72×10^{5}

$A = 0.29$ mm^2. At region around $A = 1.04$ mm^2, due to the large sensing area, the response time has slowed down ($\frac{dT}{dt}$ reduces) and $\frac{dT}{dt}$ dominates at region when $A = 1.04$ mm^2. From Fig. 7e, to get maximum pyroelectric detector performance, a sensing area in the range of 0.2 mm^2 to 0.4 mm^2 could be considered.

Based on the measured data, we first calculate the responsivity of the detector by dividing the amplitude of the measured current with the incident power at the fundamental frequency. Using the responsivity calculated and by doing Fast Fourier Transform (FFT) analysis on the dark current, we derive the Noise Equivalent Power (NEP). Specific detectivity ($D*$) is subsequently obtained by dividing the square root of the sensing area (A) with NEP as indicated by the following equation:

$$D^* = \frac{\sqrt{A}}{NEP} \tag{3}$$

Responsivity gives us the output of the pyroelectric detector with respect to the input power at 1 Hz frequency (source emitter frequency set to 1 Hz in this work), without taking into consideration the device noise. $D*$, on the other hand, takes into account the device's signal-to-noise ratio and is a better measure in comparing the pyroelectric detector's performance since device noise has been considered. As seen from (3), A has also been taken into account in the calculation of $D*$. From (3), larger A will give better $D*$ if NEP remains the same. However, NEP takes into account responsivity which in turns takes into account the device's output current. Therefore, when A gets bigger ($A = 1.04$ mm^2 as seen from Fig. 7), the reduced output current explained earlier by (1) will result in reduced responsivity, hence larger NEP.

The performance of the 4 detectors are summarized in Table I. Our best performing pyroelectric Detector 2 ($A = 0.29$ mm^2) has responsivity of 2.94×10^{-5} A/W, $NEP = 8.87 \times 10^{-9}\text{W}/\sqrt{\text{Hz}}$ and $D* = 6.04 \times 10^{6}$ cm$\sqrt{\text{Hz}}\Big/$W. The results are comparable with reported AlN pyroelectric detectors [24]. Although the specific detectivity of the best performing AlN pyroelectric detector is still around 2 orders [36] behind commercial $LiTaO_3$ pyroelectric detectors, this gap could be closed by doping the AlN pyroelectric material to increase its pyroelectric coefficient or by replacing the absorber to push absorption up to > 90%. More importantly,

the demonstration of a functional AlN pyroelectric detector fabricated at 8-inch wafer level to match as close as possible to CMOS-MEMS industry standards, gives us a glimpse towards the possibility for an 8-inch manufacturable, CMOS compatible pyroelectric detector. The lower deposition temperature for AlN ($\sim$ 200°C) compared to $LiTaO_3$ opens the flexibility to integrate these MEMS detectors with CMOS processes, which in turn expands the platform towards multi-functional, increasing the applications and functionality of pyroelectric detectors.

On-going work includes optimizing the absorption of these AlN pyroelectric detectors to expand maximum wavelength absorption in the range of 2 μm to 14 μm and doing detailed statistical analysis on the device performance uniformity over 8-inch wafer. Beyond this, we are currently in the process of integrating these pyroelectric detectors at wafer-level scale with IR emitters and waveguides via wafer-level bonding to realize monolithic integrated miniature photonics-based gas sensors.

V. Conclusion

We have demonstrated a functional pyroelectric detector that has absorption optimized to operate in the wavelength range from 5 μm to 14 μm. The pyroelectric sensing material used is AlN deposited at a temperature of around 200°C. This helps to realize CMOS-compatible, lead-free MEMS pyroelectric infrared detector, fabricated over 8-inch wafer to be as close as possible to CMOS-MEMS industry standards. The design considerations are discussed with emphasis on the absorption layer, membrane mechanical robustness and maximizing output current. These pyroelectric detectors are designed and built with the consideration to enable ease of monolithic integration with other components such as MEMS emitter and waveguides to form an integrated gas sensor system. They can therefore function as a component by itself and can also be easily integrated to be part of a gas sensor system. Pyroelectric detectors fabricated with different sensing areas are measured and the results are compared. So far, a sensing area of 0.29 mm^2 has shown to give the best performance out of the 4 sensing areas with $D^* = 6.04 \times 10^6\ cm\sqrt{Hz}/W$ and $NEP = 8.87 \times 10^{-9} W/\sqrt{Hz}$. The results from these pyroelectric detectors will form a crucial part in the design, realization and monolithic integration of architectures for CMOS-compatible miniature photonics-based gas sensors, manufactured at 8-inch wafer-level scale.

Acknowledgment

The authors thank Eva Leong for the wire-bonding service and Chong Pei Ho, Yuan Hsing Fu, Lennon Lee, Yuan Gao, and Nanxi Li for useful discussion.

References

[1] V. M. H. Ng, L. B. Kong, W. Que, C. Wang, S. Li, and T. Zhang, “Pyroelectric materials,” in *Comprehensive Energy Systems*, vol. 2. Amsterdam, The Netherlands: Elsevier, 2018, pp. 720–759.

[2] K. Yamamoto *et al.*, “Pyroelectric aluminum nitride micro electromechanical systems infrared sensor with wavelength-selective infrared absorber,” *Appl. Phys. Lett.*, vol. 104, no. 11, Mar. 2014, Art. no. 111111.

[3] E. Crisman, A. Drehman, R. Miller, A. Osinsky, D. Volovik, and V. Vasilyev, “Enhanced AlN nanostructures for pyroelectric sensors,” *Phys. Status Solidi C*, vol. 11, nos. 3–4, pp. 517–520, Mar. 2014.

[4] R. W. Whatmore, “Pyroelectric devices and materials,” *Rep. Prog. Phys.*, vol. 49, no. 12, pp. 1335–1386, Mar. 1986.

[5] B. Xiao, V. Avrutin, H. Liu, Ü. Özgür, H. Morkoç, and C. Lu, “Large pyroelectric effect in undoped epitaxial Pb(Zr,Ti)O_3 thin films on $SrTiO_3$ substrates,” *Appl. Phys. Lett.*, vol. 93, no. 5, Aug. 2008, Art. no. 052913.

[6] N. M. Shorrocks, A. Patel, M. J. Walker, and A. D. Parsons, “Integrated thin film PZT pyroelectric detector arrays,” *Microelectron. Eng.*, vol. 29, nos. 1–4, pp. 59–66, Dec. 1995.

[7] C. Giebeler *et al.*, “High performance PZT based pyro-detectors with D* of 2×109 $cmHz^{1/2}$/W for presence, gas and spectroscopy applications,” in *Proc. OPTO IRS2*, Nürnberg, Germany, 2009, pp. 185–189.

[8] P. C. A. Hammes and P. P. L. Regtien, “An integrated infrared sensor using the pyroelectric polymer PVDF,” *Sens. Actuators A, Phys.*, vol. 32, nos. 1–3, pp. 396–402, Apr. 1992.

[9] C. B. Roundy and R. L. Byer, “Sensitive $LiTaO_3$ pyroelectric detector,” *J. Appl. Phys.*, vol. 44, no. 2, p. 929, 1973.

[10] C. Ye, T. Tamagawa, P. Schiller, and D. L. Polla, “Pyroelectric $PbTiO_3$ thin films for microsensor applications,” *Sens. Actuators A, Phys.*, vol. 35, no. 1, pp. 77–83, Oct. 1992.

[11] N. Calvano, P. Chrostoski, A. Voshell, K. Braithwaite, and M. Rana, “Properties of reactively sputtered Al_xN_y thin films for pyroelectric detectors,” *Proc. SPIE*, vol. 10381, Aug. 2017, Art. no. 103810J.

[12] B. Kebede, R. A. Coutu, and L. Starman, “Optimal microelectromechanical systems (MEMS) device for achieving high pyroelectric response of AlN,” *Proc. SPIE*, vol. 8973, Mar. 2014, Art. no. 89730I.

[13] R. Hou, D. Hutson, and K. J. Kirk, “Development of sputtered AlN thin-film ultrasonic transducers for durable high-temperature applications,” *Insight-Non-Destructive Test. Condition Monitor.*, vol. 55, no. 6, pp. 302–307, Jun. 2013.

[14] J. Sebastian, “Elevated temperature sensors for on-line critical equipment health monitoring,” Univ. Dayton Res. Inst., Dayton, OH, USA, Tech. Rep. #UDR-TR-2004-00019, Apr. 2004. [Online]. Available: http://www.osti.gov/bridge/purl.cover.jsp?purl=/898359-YE6H8A/898359.pdf

[15] J. Hafner, M. Teuschel, M. Schneider, and U. Schmid, “Origin of the strong temperature effect on the piezoelectric response of the ferroelectric (co-)polymer P(VDF_{70}-$TrFE_{30}$),” *Polymer*, vol. 170, pp. 1–6, Apr. 2019.

[16] G. A. Gavrilov *et al.*, “Studying the pyroelectric effect in AlN epilayers,” *Tech. Phys. Lett.*, vol. 44, no. 8, pp. 709–712, Aug. 2018.

[17] G. E. Stan, M. Botea, G. A. Boni, I. Pintilie, and L. Pintilie, “Electric and pyroelectric properties of AlN thin films deposited by reactive magnetron sputtering on Si substrate,” *Appl. Surf. Sci.*, vol. 353, pp. 1195–1202, Oct. 2015.

[18] V. Fuflyigin, E. Salley, A. Osinsky, and P. Norris, “Pyroelectric properties of AlN,” *Appl. Phys. Lett.*, vol. 77, no. 19, pp. 3075–3077, Nov. 2000.

[19] W. S. Yan *et al.*, “Temperature dependence of the pyroelectric coefficient and the spontaneous polarization of AlN,” *Appl. Phys. Lett.*, vol. 90, no. 21, May 2007, Art. no. 212102.

[20] E. E. Crisman, J. S. Derov, A. J. Drehman, and O. J. Gregory, “Large pyroelectric response from reactively sputtered aluminium nitride thin films,” *Electrochem. Solid-State Lett.*, vol. 8, no. 3, pp. H31–H32, Jan. 2005.

[21] D. Popa and F. Udrea, “Towards integrated mid-infrared gas sensors,” *Sensors*, vol. 19, no. 9, p. 2076, May 2019.

[22] J. W. Stewart, J. H. Vella, W. Li, S. Fan, and M. H. Mikkelsen, “Ultrafast pyroelectric photodetection with on-chip spectral filters,” *Nature Mater.*, vol. 19, no. 2, pp. 158–162, Feb. 2020.

[23] S. P. Gaur, K. Rangra, and D. Kumar, “MEMS AlN pyroelectric infrared sensor with medium to long wave IR absorber,” *Sens. Actuators A, Phys.*, vol. 300, Dec. 2019, Art. no. 111660.

[24] C. Ranacher *et al.*, “A CMOS compatible pyroelectric mid-infrared detector based on aluminium nitride,” *Sensors*, vol. 19, no. 11, p. 2513, May 2019.

[25] H. Lin *et al.*, “Mid-infrared integrated photonics on silicon: A perspective,” *Nanophotonics*, vol. 7, no. 2, pp. 393–420, Feb. 2018.

[26] N. Li *et al.*, “Radiation enhancement by graphene oxide on microelectromechanical system emitters for highly selective gas sensing,” *ACS Sensors*, vol. 4, no. 10, pp. 2746–2753, Sep. 2019.

[27] T. Hu *et al.*, “Silicon photonic platforms for mid-infrared applications,” *Photon. Res.*, vol. 5, no. 5, pp. 417–430, Aug. 2017.

[28] C. Consani, C. Ranacher, A. Tortschanoff, T. Grille, P. Irsigler, and B. Jakoby, "Mid-infrared photonic gas sensing using a silicon waveguide and an integrated emitter," *Sens. Actuators B, Chem.*, vol. 274, pp. 60–65, Nov. 2018.

[29] M. S. Yazici, B. Dong, D. Hasan, F. Sun, and C. Lee, "Integration of MEMS IR detectors with MIR waveguides for sensing applications," *Opt. Express*, vol. 28, no. 8, pp. 11524–11537, Apr. 2020.

[30] A. A. Irudayaraj, R. Srinivasan, P. Kuppusami, E. Mohandas, S. Kalainathan, and K. Ramachandran, "Photoacoustic measurement of thermal properties of TiN thin films," *J. Mater. Sci.*, vol. 43, no. 3, pp. 1114–1120, Feb. 2008.

[31] M. K. Samani *et al.*, "Thermal conductivity of titanium nitride/titanium aluminum nitride multilayer coatings deposited by lateral rotating cathode arc," *Thin Solid Films*, vol. 578, pp. 133–138, Mar. 2015.

[32] K. R. Williams, K. Gupta, and M. Wasilik, "Etch rates for micromachining processing—Part II," *J. Microelectromech. Syst.*, vol. 12, no. 6, pp. 761–777, Dec. 2003.

[33] A. Hossain and M. H. Rashid, "Pyroelectric detectors and their applications," *IEEE Trans. Ind. Appl.*, vol. 27, no. 5, pp. 824–829, Oct. 1991.

[34] J. Kischkat *et al.*, "Mid-infrared optical properties of thin films of aluminum oxide, titanium dioxide, silicon dioxide, aluminum nitride, and silicon nitride," *Appl. Opt.*, vol. 51, no. 28, pp. 6789–6798, Oct. 2012.

[35] M. M. Kirillova, L. V. Nomerovannaya, and M. M. Noskov, "Optical properties of molybdenum single crystals," *Sov. Phys. JETP*, vol. 33, no. 6, pp. 1210–1214, Dec. 1971.

[36] Infratec. *Datasheet LME-351*. Accessed: Aug. 2, 2020. [Online]. Available: https://www.infratec-infrared.com/downloads/en/sensor-division/detector_data_sheet/infratec-datasheet-lme-351-_.pdf

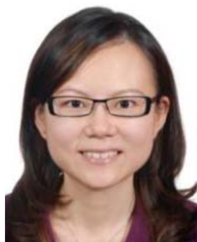

Doris K. T. Ng received the Ph.D. degree in engineering from the National University of Singapore (NUS), Singapore, in 2008.

She joined Agency for Science, Technology and Research (A∗STAR) in 2007 and worked on integrated photonics for more than ten years from devices and platforms to applications for datacom, data storage, sensing, and instrumentation. She has been taking a major role in the development of integrated photonics infrastructure and innovative technologies towards photonic subsystem-on-chip, including compact heterogeneous III–V/Si photonic platform, on-chip lasers, fiber-to-chip coupling, and high-efficiency light delivery system for on-chip near-field energy transfer. Her research interests include electronic-photonic integration and materials development for non-linear optics. Her key achievements include high-efficiency heterogeneous Si/III–V integration with short optical vertical interconnect access, ultra-high refractive index silicon-rich nitride for non-linear optics applications and a simple one-step direct deposition of ultra-smooth metal film deposition for nanoplasmonic applications. These work were reported and highlighted in Asia Research News, Laser focus World, Novus Light Technologies, and Photonic Spectrum.

Dr. Ng is currently working on photonics-based gas sensors, pyroelectric infrared detectors, and study of novel piezoelectric materials.

Guoqiang Wu (Member, IEEE) received the B.Eng. degree in electrical science and technology from Xidian University, Xi'an, China, in 2008, and the Ph.D. degree in microelectronics and solid-state electronics from the Shanghai Institute of Microsystem and Information Technology (SIMIT), Chinese Academy of Sciences, Shanghai, China, in 2013.

From 2011 to 2018, he was a Research Scientist with the Institute of Microelectronics, Agency for Science, Technology and Research (A∗STAR), Singapore. He is currently a Professor with The Institute of Technological Sciences, Wuhan University, Wuhan, China. His research interests include microelectromechanical system (MEMS) design and integration.

Dr. Wu was a recipient of the Best Dissertation Award of Shanghai in 2014.

Tan-Tan Zhang received the B.Sc. degree in automation from Fuzhou University, Fuzhou, China, the M.Sc. and Ph.D. degrees in E.E.E. (now E.C.E) from the University of Macau, Macao, China. He was as a Research Assistant with the State Key Laboratory of Analog and Mixed-Signal VLSI from 2010 to 2018. He took short-term internship with SICK AG, Waldkirch, Germany, in 2007. He has been the Institute of Microelectronics (IME), A∗STAR, Singapore, as a Research Scientist, since 2018. His current research interests include ultra-low power circuits and systems for biomedical applications and energy-efficient sensor interfaces. He was a recipient of the Student Travel Granted Award of the IEEE International Solid-State Circuits Conference in 2017.

Linfang Xu received the bachelor's and master's degrees in electrical engineering from Xi'an Jiaotong University, China, in 2000 and 2003, respectively.

She was as a Senior Research and Development Engineer with Philips Electronics Singapore. She is currently a Senior Research Engineer with the Institute of Microelectronics, A∗STAR, Singapore. Her current research interests include photonics based gas sensor, sensor signal processing, and software algorithm. She has published more than ten international scientific articles and patents.

Jianbo Sun received the B.S. degree in mechanical engineering from the Huazhong University of Science and Technology, Wuhan, China, in 2001, and the Ph.D. degree from Nanyang Technological University, Singapore, in 2006.

He joined as a Research Scientist with the Institute of Microelectronics, Singapore, in 2016. He is currently working with HiSilicon as a Technique Expert.

Wing-Wai Chung received the B.Eng. degree in electrical and electronics engineering from Nanyang Technological University, Singapore, in 2004, and the M.S. degree in electrical engineering from National University of Singapore, Singapore, in 2011.

From 2011 to 2014, he was a Research Engineer with the Nano-Electronics Program, Institute of Microelectronics, Singapore. From 2014 to 2018, he was a Research Engineer with the MEMS-Integration and Projects Program, Institute of Microelectronics, Singapore. Since 2018, he has been a Senior Research Engineer with the Sensors, Actuators, and Microsystems Program, Institute of Microelectronics, Singapore. His research interest includes process integration and fabrication of microelectromechanical systems.

Hong Cai received the B.Eng. degree from Xi'an Jiaotong University, Xi'an, China, in 1997, and the M.Eng. and Ph.D. degrees in electrical and electronics engineering from Nanyang Technological University, Singapore, in 2002 and 2009, respectively.

Since 2009, She has been with the Institute of Microelectronics, Agency for Science, Technology and Research (A∗STAR), Singapore, as a Research Scientist. Her research is related to photonics technology and development. Her main research interests include integrated photonics, quantum photonics, optoelectronics, optomechanics, and NEMS/MEMS. Also, over the past 20 years, She has been focused on photonics platform development and sensors applications.

Qingxin Zhang received the B.S. and M.E. degrees in semiconductors devices and physics from the Harbin Institute of Technologies, China, in 1986 and 1989, respectively, and the Ph.D. degree in microelectronics from the Institute of Microelectronics, Tsinghua University, China, in 1997. After two years as a Research Fellow with Nanyang Technology University, Singapore, he joined the Institute of Microelectronics, Singapore, in 1999, where he is currently a Senior Scientist working with the Sensors, Actuators, and Microsystem Program. He has authored or coauthored more than 100 peer-reviewed journal and conference papers and has filed more than ten technology disclosures. His current interests are MEMS process integration, and platform technologies development in the areas of RF MEMS, integrated gas sensors, and SiC power devices.

Navab Singh received the M.Tech. degree in solid state materials from the Indian Institute Technology, Delhi (IITD) and the Ph.D. degree in electrical and computer engineering from NUS. He spent last 24 years in semiconductor research and has authored or coauthored more than 200 technical articles (citations more than 3000 and H-index more than 30) in referred archival journals and conferences and has filed more than 20 technology disclosures. He was a recipient of the George E. Smith Award 2007 for Best Paper in the IEEE ELECTRON DEVICE LETTERS, the Singapore National Technology Award 2008 for his outstanding contributions to the research and development of nanowire-technology platform, enabling the realization of ultimately scaled CMOS integrated circuits and new class of electronic bio-sensors, the IME Excellence Award 2009 for industry project developing Surround Gate Transistor (SGT) technology, and the A∗STAR TALENT Award 2010 for Leading, Educating, and Nurturing Talents.